A new approach to the real-time assessment of the clear-sky direct normal irradiance

Julien Nou, Rémi Chauvin, Stéphane Thil, Stéphane Grieu

A new approach to the real-time assessment of the clear-sky direct normal irradiance

Julien Nou[a], Rémi Chauvin[a], Stéphane Thil[a,b], Stéphane Grieu[a,b,*]

[a] *PROMES-CNRS (UPR 8521), Rambla de la thermodynamique, Tecnosud, 66100 Perpignan, France*
[b] *Université de Perpignan Via Domitia, 52 Avenue Paul Alduy, 66860 Perpignan, France*

Abstract

In a context of sustainable development, interest for concentrating solar power and concentrating photovoltaic technologies is growing rapidly. One of the most challenging topics is to improve solar resource assessment and forecasting in order to optimize power plant operation. Since clear sky defines the nominal operating conditions of the plants, improving their management requires the use in real-time of clear-sky direct normal irradiance (DNI) models. Typically, accuracy is best achieved by considering water vapor and aerosol concentrations in the atmosphere separately. However, measuring such physical quantities is not easy and requires a weather station close to the considered site. When these data are not available, the attenuating effects can be modelled by atmospheric turbidity factors which can be obtained from DNI under clear-sky conditions. So, the main purpose of the present paper is to propose an efficient approach to assess the clear-sky DNI in real time. This approach combines an existing empirical model, proposed by Ineichen and Perez, with a new methodology for the computation of atmospheric turbidity. It takes advantage of the fact that changes in atmospheric turbidity are relatively small throughout the day in comparison to changes in DNI, even when the sky is free of clouds. In the present study, we considered data from two experimental sites (Golden, in the USA, and Perpignan, in France) and used a wavelet-based multi-resolution analysis as a clear-sky DNI detection tool. In addition, we compared the proposed approach with several combinations of empirical models and ways of computing atmospheric turbidity. The first model is a polynomial of the cosine of the solar zenith angle, whereas the two other models use atmospheric turbidity as an additional input. Regarding its calculation, monthly and daily mean values have been considered. Moreover, we defined a procedure in order to evaluate the accuracy of all the considered approaches. This procedure allows changes in DNI caused by clouds to be simulated using a noisy signal applied to clear-sky periods. In both sites, our approach to the real-time assessment of the clear-sky DNI outperforms the other approaches. In the worst case, the mean absolute error is reduced by 8 W m^{-2} in comparison to the approaches based on monthly mean values of atmospheric turbidity, and reduced by about 30 W m^{-2} when taking the polynomial-based model as a reference.

Keywords: clear-sky DNI model, atmospheric turbidity, solar zenith angle, real-time assessment, concentrating solar power.

1. Introduction

Nowadays, solar technologies like concentrating solar power (CSP) are becoming an important source of renewable energy in countries like Spain and USA and can potentially be used at a very large scale in many other countries (Arvizu et al., 2011). However, the main drawback of CSP remains its cost. A better real-time management of the CSP plants is therefore essential in order to improve their competitiveness against classical power plants. So, one of the most challenging topics is to improve the solar resource assessment and forecasting so as to optimize power plant operation. Indeed, in CSP plants, electricity generation is directly impacted by the availability and variability of the solar resource and, more specifically, by direct normal irradiance (DNI). DNI can be defined as the direct irradiance received on a plane normal to the Sun (Blanc et al., 2014). It is the relevant component of the solar irradiance for CSP applications and can be split into two multiplicative terms: the clear-sky DNI (I_{cs}) and the clearness index (k_t). I_{cs} represents the solar power received at ground level per unit of area, at a specific location, when there is no cloud occulting the Sun. This is a key information since it is directly related to the upper limit of the available solar energy. k_t is derived from the attenuation of the clear-sky DNI caused by clouds. It spans from 0, when a thick cloud is occulting the Sun, to 1, when there is no cloud occulting the Sun.

Having access to forecasted values of DNI could help operators to improve the operational strategies of the plants, for instance by adapting in real time the flow rate of the heat transfer fluid in parabolic trough power plants. This flow rate must be kept above a minimum level to avoid overheating the tubes and damaging them significantly. Regarding CSP towers, having access to forecasted values of DNI could have a part in the improvement of the aim point strategies used in that plants. This could also contribute to lower the cost related to grid integration. In both cases, operators are often willingly overestimating the solar resource to prevent possible damage to the plants, which results in a reduced efficiency. Consequently, efficient forecasting tools are needed to optimize power plant operation.

In the field of real-time solar resource assessment and forecasting, sky-imaging systems are of particular interest due to their ability to provide information about the sky conditions

*Corresponding author
Email address: stephane.grieu@promes.cnrs.fr (Stéphane Grieu)

Nomenclature		
b	Coefficient defined as a function of the altitude of the considered site	-
d	Sun-Earth distance	km
d_0	Mean Sun-Earth distance	km
dec	Decision coefficient (equal to 1 when there is no cloud occulting the Sun, 0 otherwise)	-
doy	Day of year, ranging from 1 (January 1st) to 365 (December 31)	-
h	Altitude of the considered site	m
k_{rand}	Random value used in the evaluation of the considered approaches (between 0 and 1)	-
k_t	Clearness index	-
m	Relative optical air mass	-
m_p	Relative optical air mass corrected by the altitude of the site	-
p	Number of data used in the evaluation of the considered approaches	-
t_{past}	Time of the last trustworthy atmospheric turbidity value	s
t_w	Length of the temporal window used in the detection process of clear-sky DNI data	min
v	Pseudo-random binary sequence used in the evaluation of the considered approaches	-
w	Pseudo-random binary sequence containing only a part of the detected clear-sky periods	-
z	Solar zenith angle	$^\circ$
C_T	Coefficient of turbidity	-
D	Sum of all details coefficients for the clear-sky DNI data detection process	W m^{-2}
I	Direct normal irradiance (DNI)	W m^{-2}
I_{cs}	Clear-sky DNI	W m^{-2}
$I_{cs_{max}}$	Maximum value of the clear-sky DNI in the considered database	W m^{-2}
$I_{cs_{min}}$	Minimum value of the clear-sky DNI in the considered database	W m^{-2}
$\hat{I}_{cs}$	Estimated clear-sky DNI	W m^{-2}
I_g	Generated sequence of DNI values	W m^{-2}
I_0	Extraterrestrial solar irradiance	W m^{-2}
I'_0	Solar constant	W m^{-2}
L	Level of decomposition	-
MAE	Mean absolute error	W m^{-2}
N	Polynomial order	-
NRMSE	Normalized root mean square error	%
$R_{0/1}$	Ratio of data kept among the detected clear-sky DNI data	-
T_{max}	Maximum value of atmospheric turbidity (specific to the considered database)	-
T_{min}	Minimum value of atmospheric turbidity (specific to the considered database)	-
T_L	Atmospheric turbidity, as defined by Linke (Linke, 1922)	-
T_{LI}	Atmospheric turbidity, as defined by Ineichen and Perez (Ineichen and Perez, 2002)	-
T_{LK}	Atmospheric turbidity, as defined by Kasten (Kasten, 1980)	-
T_{LK2}	Atmospheric turbidity, as defined by Kasten, for an air mass equal to 2	-
$T^\star_{LI}$	Atmospheric turbidity, as computed using the methodology described in Section 6	-
$\langle T_{LI} \rangle_{m/d}$	Monthly/daily mean value of atmospheric turbidity	-
α	Maximum growth rate of atmospheric turbidity	s^{-1}
β	Threshold value involved in the computation of $T^\star_{LI}$	-
δ_{cda}	Optical thickness of a water- and aerosol-free atmosphere (clean and dry atmosphere)	-
η_{cs}	Index of clear-sky data detection	%
η_{md}	Percentage of clear-sky data missed by the detection algorithm	%
η_{id}	Percentage of data incorrectly considered as clear-sky data	%
μ	Moving average value computed from the detail signal of DNI	W m^{-2}
μ_{max}	Maximum accepted value of μ for the selection of clear-sky DNI data	W m^{-2}
τ	Optical depth of the atmosphere	-
ΔT_{max}	Largest admissible change in atmospheric turbidity	-

at high temporal and high spatial resolutions (Bernecker et al., 2014; Chauvin et al., 2014). These systems are mainly used to forecast the clearness index (k_t). Regarding the clear-sky DNI (I_{cs}), on which the present paper focuses, models are divided into two categories: radiative transfer models and empirical models (Gueymard, 2012a; Engerer and Mills, 2015; Gueymard and Ruiz-Arias, 2015). In radiative transfer models, the clear-sky DNI is usually derived from the Beer-Lambert law (Eq. (1)):

$$I_{cs} = I_0 \cdot e^{-m\tau} \tag{1}$$

where m is the relative optical air mass and τ is the optical depth of the atmosphere. Note that τ is a key parameter in accu-

rately assessing the state of the atmosphere and, consequently, the amount of solar energy reaching the ground (Davies and McKay, 1982; Gueymard, 2008; Gueymard and Myers, 2008). It is expressed as the sum of the broadband transmittances due to Rayleigh scattering (τ_{Ra}), uniformly mixed gases absorption (τ_g), ozone absorption (τ_{O_3}), nitrogen dioxide absorption (τ_{NO_2}), water vapor absorption (τ_{H_2O}), and aerosol extinction (τ_A). Among all the radiative models one can find in the literature, REST2 (Gueymard, 2008) has proven to assess DNI with unsurpassed accuracy. Highly complex phenomena that involve interactions between atmospheric particles (e.g. aerosols and water vapor) and sunbeams are considered in that model. In addition, REST2 includes two spectral bands with distinct transmission and scattering properties. Although radiative transfer models often produce better estimates of the clear-sky DNI than empirical models, they need input data that might be not available at any time. Indeed, aerosol optical depth data are required but happen to be difficult to obtain, as well as rarely available (Gueymard, 2012c). As a consequence, radiative transfer models are not suitable for real-time applications.

Regarding empirical models, several levels of complexity can be distinguished. First, in a recent work on the forecasting of intra-hour DNI, the clear-sky DNI was simply assumed to be constant over the tested period and equal to 900 $\mathrm{W\,m^{-2}}$ (Marquez and Coimbra, 2013a). Excluding this, the simplest clear-sky DNI models are usually based on the solar zenith angle and empirical correlations derived from experimental measurements. As an example, one can mention the Daneshyar-Paltridge-Proctor model (Paltridge and Proctor, 1976; Daneshyar, 1978) or the Meinel Model (Meinel and Meinel, 1976). The clear-sky DNI can also be computed from an eight-order polynomial of the cosine of the solar zenith angle (Chu et al., 2013; Quesada-Ruiz et al., 2014) but, using this kind of expression, two different years are necessarily modelled in the same way. Due to changes in climate and atmospheric conditions from a year to another, this is of course not representative of what truly happens. Another model, proposed by Laue (Laue, 1970), takes the altitude of the site into consideration, in addition to the solar zenith angle. In general terms, accuracy of these models is negatively impacted by the lack of information about the state of the atmosphere. So, these past few years, several studies have been dedicated to developing more efficient models (Chow et al., 2011; Yang et al., 2014; Chu et al., 2015). Basically, these models use atmospheric turbidity, which can be determined from broadband beam radiation measurements, as an additional input (Ineichen and Perez, 2002). However, in these models, information about the state of the atmosphere is not real-time information and is generally derived from mean values or approximations provided by solar energy services (SoDa, 2015). Because atmospheric turbidity can be quite variable over the days, accuracy of the models can be unsatisfactory, especially at high solar zenith angles.

In either case, models need to be validated through a comparison between the estimates they produce and measurements. This is an offline phase and, as a consequence, a set of clear-sky DNI data must be available. These data can be manually selected within a database of DNI measurements or collected using a detection algorithm. Typically, one can use direct filtering of cloud conditions in the DNI time series (Long and Ackerman, 2000) or back-end filtering (Gueymard, 2013). Using the latter, all of the DNI data is considered and observations that provide physically-unreasonable clear-sky conditions are removed. Another possibility lies in using the andogenous statistical model developed by Reno et al. (Reno et al., 2012). In this sense, Inman et al. proposed a clear-sky detection algorithm based on this model (Inman et al., 2015). The authors focused on the sensitivity of day-ahead clear-sky DNI forecasts to local fluctuations in atmospheric turbidity. They used average daily Linke turbidity factors to correct for temporally and spatially local aerosol loading and water vapor content.

In a previous work (Nou et al., 2014), a multi-resolution analysis based on the discrete wavelet transform has been devoted to the same purpose. Such a methodology has proven to be relevant for offline detection of clear-sky DNI data in large datasets and is therefore useful for data preprocessing and model development. However, the algorithm did not perform well when only the first hours of the day are available: the whole day is needed. Limitations of the algorithm occured in case of some very cloudy periods. That is why some improvements have been realized in order to detect clear-sky DNI data with higher accuracy.

The main purpose of the present paper is to propose an efficient approach to the real-time assessment of the clear-sky DNI. It combines an existing empirical model with a new methodology for the computation of atmospheric turbidity. This methodology relies on a persistence of atmospheric turbidity at short notice and takes advantage of the fact that changes in this quantity are relatively small throughout the day in comparison to changes in DNI, even when the sky is free of clouds. So, atmospheric turbidity is computed using the last detected clear-sky DNI measurement. Data from two experimental sites (Golden, in the USA, and Perpignan, in France) are used to compare the proposed approach with several combinations of empirical clear-sky DNI models and ways of computing atmospheric turbidity. A polynomial of the cosine of the solar zenith angle is also included in the comparative study. An evaluation procedure, allowing changes in DNI caused by clouds to be simulated using a noisy signal applied to clear-sky periods, is proposed.

The paper is organized as follows: Section 2 introduces some considerations on the computation of the position of the Sun, the extraterrestrial irradiance, and the relative optical air mass. In particular, several functional forms one can use for approximating the relative optical air mass are presented. Section 3 discusses all the considered combinations of empirical models and ways of calculating atmospheric turbidity, including the proposed approach. The databases of DNI measurements are presented in Section 4, as well as the characteristics of the two experimental sites. Section 5 details how clear-sky DNI data are extracted from these databases by using a multi-resolution analysis based on the discrete wavelet transform. As mentioned above, this step is essential in the development and validation of the proposed approach. Section 6 focuses on the methodology proposed for the computation of atmospheric turbidity. Section 7 is about the evaluation procedure when both the tuning of the models and results are presented in Section 8. The paper ends with a conclusion and an outlook to future work.

Table 1: Characteristics of existing algorithms for computing the Sun's angles.

Characteristics	SPA	SG	MICH	ENEA	SG2
Validity range (years)	[−2000 ; 6000]	[1980 ; n/a]	[1950 ; 2050]	[2003 ; 2022]	[1980 ; 2030]
Uncertainty [°]	0.0003	0.2	0.01	0.001	< 0.001
Additions	1000	25	20	40	–
Multiplications	1300	35	35	40	–
Calls	300	25	25	25	–
Computation time [s]	t_{SPA}	$t_{\mathrm{SPA}}/15$	$t_{\mathrm{SPA}}/20$	$t_{\mathrm{SPA}}/20$	$< t_{\mathrm{SPA}}/20$

2. Opening remarks

2.1. Position of the Sun

The knowledge of the Sun-Earth geometry is essential in the developement of a clear-sky DNI model. Location (latitude, longitude and altitude) and time are required to determine the solar azimuth and zenith angles (Figure 1). Computing these two angles is not trivial because it involves multiple phenomena (Earth rotation and declination, spatial coordinates, etc.).

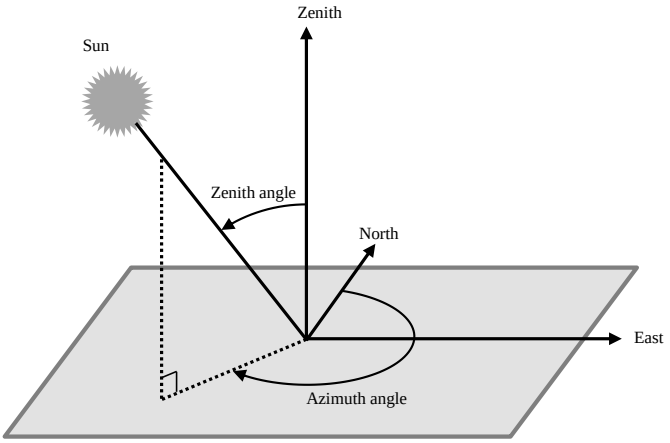

Figure 1: Representation of azimuth and zenith angles.

The existing algorithms show differences in terms of computation time, accuracy and time period definition to compute these solar angles. Among the best known algorithms developed for computing the Sun's angles, one can cite the Sun Position Algorithm, called SPA (Reda and Andreas, 2003, 2004) and developed at the National Renewable Energy Laboratory (NREL). This algorithm calculates the solar azimuth and zenith angles for a very large period (from the year −2000 to 6000) with uncertainties of about 1" (0.0003°). However, due to approximately 2300 operations, and more than 300 calls of trigonometric functions needed to calculate one solar position, the computation cost is high. A faster algorithm, called SG for Solar Geometry (Wald, 2007), has been developed for the European Solar Radiation Atlas. It can be applied during the time period starting from 1980 and requires, for one solar position, approximately 60 operations, and 25 calls of trigonometric functions. The SG algorithm is about 15 times faster than SPA. Two other algorithms, more than 20 times faster than SPA have been developed with acceptable uncertainties. Indeed, the algorithm called MICH (Michalsky, 1988), taken from *The Astronomical Almanac*, offers a root mean square error of approximately 40" (0.01°). It can be applied during the period 1950-2050 and requires, for one solar position, approximately 55 operations and 25 calls of trigonometric functions. Regarding the algorithm proposed by Grena (Grena, 2008) and called ENEA, it can be applied during the period 2003-2022 and requires, for one solar position, approximately 80 operations, and 25 calls of trigonometric functions. It offers a root mean square error of approximately 4" (0.001°). Finally, another algorithm called SG2 (Blanc and Wald, 2012), faster than the SPA, MICH, and ENEA algorithms, provides the same level of accuracy achieved by ENEA but extended to the period 1980-2030. Each algorithm offers acceptable computation speed and accuracy with regard to the application needs.

In this work, we decided for the SG2 algorithm because it is accurate and fast enough (Table 1). In addition, it allows the Sun-Earth distance, which is essential in the developed approach, to be computed at each time step.

2.2. Extraterrestrial solar irradiance

The extraterrestrial solar irradiance I_0 is defined as the power per square meter reaching the top of the Earth's atmosphere on a surface normal to the beam. Due to the elliptical orbit of the Earth, the extraterrestrial solar irradiance I_0 is not constant and varies through the year as follows (Eq. (2)):

$$I_0 = (d_0/d)^2 \cdot I'_0 \tag{2}$$

where I'_0 is the solar constant defined as the average extraterrestrial solar irradiance at mean Sun-Earth distance (d_0 = 149 597 871 km). The ratio d_0/d comes from the conservation of flux and is given by the SG2 algorithm. Regarding the solar constant I'_0, Gueymard proposed in 2004 a value of 1366.1 W m^{-2} by using the most recent composite time series of total solar irradiance spaceborne measurements (Gueymard, 2004). In 2012, this value has been corrected after detecting a systematic bias in the data. So, I'_0 is now set to 1361.2 W m^{-2} (Gueymard, 2012b). Several empirical expressions, available in the literature, approximate Eq. (2). As an example, I_0 can be computed using a very simple expression given by Eq. (3) (Duffie and Beckman, 1980):

$$I_0 = (1 + 0.0334 \cos(2\pi \cdot doy/365)) \cdot I'_0 \tag{3}$$

where *doy* is the day of year, ranging from 1 (January 1$^{\mathrm{st}}$) to 365 (December 31). Although this formulation may be employed for most engineering and technological applications, the first expression has been preferred due to the availability of the variable d in the used databases.

2.3. Relative optical air mass

The relative optical air mass, noted m, is also a key parameter in clear-sky DNI models. It corresponds to the ratio of the optical path length of the solar beam through the atmosphere to the optical path through a standard atmosphere at sea level with the Sun at the zenith. In addition, both the Earth's curvature and the variable density of the atmosphere induce a longer path for the beam, especially with high solar zenith angles (when the Sun is near the horizon), where the path length increases (Figure 2).

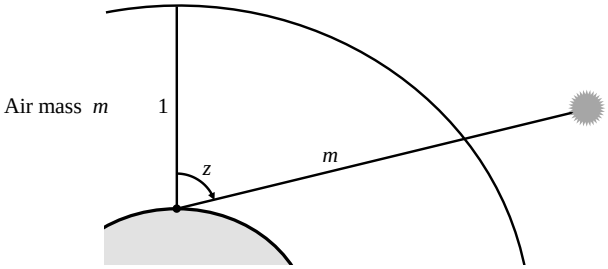

Figure 2: Representation of the air mass.

The solar position must be known in order to calculate the relative optical air mass. If the Earth's curvature and the atmosphere optical effects are neglected, the relative optical air mass can be expressed using Eq. (4), where z is the solar zenith angle (parallel plate approximation):

$$m = \frac{1}{\cos z} \tag{4}$$

This formulation is wrong at high zenith angles because, in that case, air mass increases dramatically, and even tends to infinity at 90°. That is why many formulations based on both measured data and solar zenith angle have been proposed. In 2011, Rapp-Arrarás and Domingo-Santos made a very exhaustive review and systematic comparison of functional forms for approximating the relative optical air mass at any solar zenith angle (Rapp-Arrarás and Domingo-Santos, 2011). Four of the most famous are recalled below.

First, Young and Irvine proposed a formulation which is more appropriate than the parallel plate approximation for zenith angles between 83° and 87° (Young and Irvine, 1967). However, at 90°, this functional form still diverges (Eq. (5)):

$$m = \frac{1}{\cos z}\left[1 - 0.0012\left(\frac{1}{\cos^2 z} - 1\right)\right] \tag{5}$$

In spite of this limitation, it led to the development of several other formulations, among which two that Young was involved in developing. The first one (Kasten and Young, 1989) is defined as follows (Eq. (6)):

$$m = \frac{1}{\cos z + 0.50572 \cdot (96.07995 - z)^{-1.6364}} \tag{6}$$

The second one (Young, 1994) is expressed by Eq. (7), with a the cosine of the solar zenith angle:

$$m = \frac{1.002432\, a^2 + 0.148386\, a + 0.0096467}{a^3 + 0.149864\, a^2 + 0.0102963\, a + 0.000303978} \tag{7}$$

Gueymard also proposed a modified formulation of the relative optical air mass (Gueymard, 1993). He defined in the following way this key parameter in clear-sky DNI models (Eq. (8)):

$$m = \frac{1}{\cos z + 0.00176759 \cdot z \cdot (94.37515 - z)^{-1.21563}} \tag{8}$$

Figure 3 provides an overview of these five functional forms. Overall, they present very similar results for solar zenith angles below 80° (which corresponds to the operating conditions of a solar power plant). As a result, a simple formulation like the parallel plate approximation (Eq. (4)) could have been enough. However, for its accuracy at all zenith angles and because the computations are very fast (a few milliseconds), the formulation proposed by Kasten and Young has been selected (Eq. (6)).

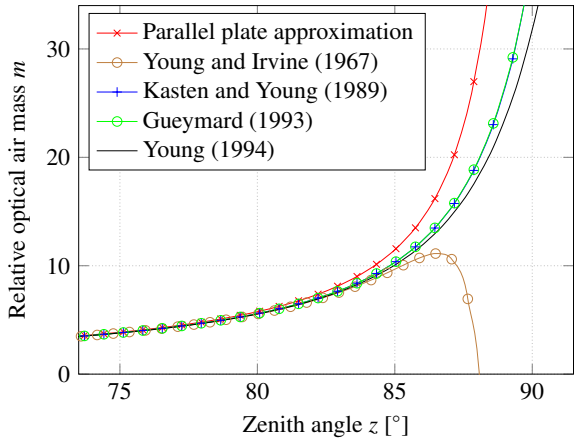

Figure 3: Overview of five air mass formulations.

3. Real-time assessment of the clear-sky DNI

In this section are presented the selected empirical models, the approaches included in the comparative study, and the approach proposed to the real-time assessment of the clear-sky DNI.

3.1. Selected empirical models

Among all the empirical clear-sky DNI models highlighted in the introduction section, we selected first a polynomial of the cosine of the solar zenith angle (Chu et al., 2013; Quesada-Ruiz et al., 2014). It is defined by Eq. (9):

$$\hat{I}_{cs} = \sum_{n=0}^{N} a_n \cdot (\cos z)^n \tag{9}$$

where the coefficients $\{a_n\}_{0 \leqslant n \leqslant N}$ can be obtained by using the least-squares method (Section 8.1.2). Note that in this paper $\hat{I}_{cs}$ stands for estimates of the clear-sky DNI whereas I_{cs} represents the clear-sky DNI, in a more general way. The other models considered in the comparison study are derived from works realized by Linke. In 1922, he proposed to express DNI as a function of the total optical thickness of a cloudless atmosphere (Linke, 1922), which is defined as the product of the optical thickness of a water- and aerosol-free atmosphere (a clear and

dry atmosphere) (δ_{cda}) and the Linke turbidity coefficient (T_L) (Eq. (10)):

$$\hat{I}_{cs} = I_0 \cdot \exp\left(-\delta_{cda} \cdot T_L \cdot m\right) \tag{10}$$

As a result, depending on the way the theoretical value of δ_{cda} is computed, the evaluation of T_L can be different. Note that T_L is the number of clean dry atmospheres leading to the observed attenuation of solar irradiance. In 1980, Kasten proposed the following formulation (Kasten, 1980), which is known as the *Kasten's pyrheliometric formula* and widely used by the scientific community (Eq. (11)):

$$\delta_{cda}^{K} = (9.4 + 0.9 \cdot m)^{-1} \tag{11}$$

The corresponding Kasten-reviewed Linke turbidity coefficient (T_{LK}) is then obtained as follows (Eq. (12)):

$$T_{LK} = \ln\left(I_0/I_{cs}\right) \cdot (9.4 + 0.9 \cdot m)\,/m \tag{12}$$

After new measurement campaigns, other formulations of δ_{cda} have been proposed. All of them are based on a fourth-order polynomial of the air mass (Louche et al., 1986; Grenier et al., 1994; Kasten, 1996). Among these works, one can highlight the new formulation proposed by Kasten. It is used to estimate the solar radiation at ground level from satellite images in the framework of the new digital European Solar Radiation Atlas (ESRA) (Rigollier et al., 2000) and is given by Eq. (13):

$$\delta_{cda}^{ESRA} = \frac{10^4}{66296 + 17513m_p - 1202m_p^2 + 65m_p^3 - 1.3m_p^4} \tag{13}$$

where m_p is equal to the relative optical air mass defined by Eq. (6) corrected by the altitude of the considered site (Eq. (14)):

$$m_p = m \cdot \exp\left(-h/8434.5\right) \tag{14}$$

The corresponding clear-sky DNI model is given by Eq. (15):

$$\hat{I}_{cs} = I_0 \cdot \exp\left(-0.8662 \cdot m_p \cdot \delta_{cda} \cdot T_{LK2}\right) \tag{15}$$

where T_{LK2} is the Kasten-reviewed Linke turbidity coefficient for an air mass equal to 2. Although the Kasten-reviewed Linke turbidity coefficient is easy to calculate, it has a strong dependence on air mass (Kasten, 1988; Kasten and Young, 1989; Grenier et al., 1994; Eltbaakh et al., 2012), which is problematic. That is why Ineichen and Perez proposed in 2002 a new formulation of the atmospheric turbidity coefficient in order to limit this dependence (Ineichen and Perez, 2002). In this work, they also defined b as a function of the altitude of the considered site. The model they developed is given by Eq. (16):

$$\hat{I}_{cs} = b \cdot I_0 \cdot \exp\left(-0.09 \cdot m\left(T_{LK2} - 1\right)\right) \tag{16}$$

where b is expressed as follows (Eq. (17)):

$$b = 0.664 + \frac{0.163}{\exp\left(-h/8000\right)} \tag{17}$$

So, the atmospheric turbidity coefficient revised by Ineichen and Perez (T_{LI}) (Eq. (18)) can be computed by inverting Eq. (16):

$$T_{LI} = 1 + \left[\frac{11.1}{m} \cdot \ln\left(\frac{b \cdot I_0}{I_{cs}}\right)\right] \tag{18}$$

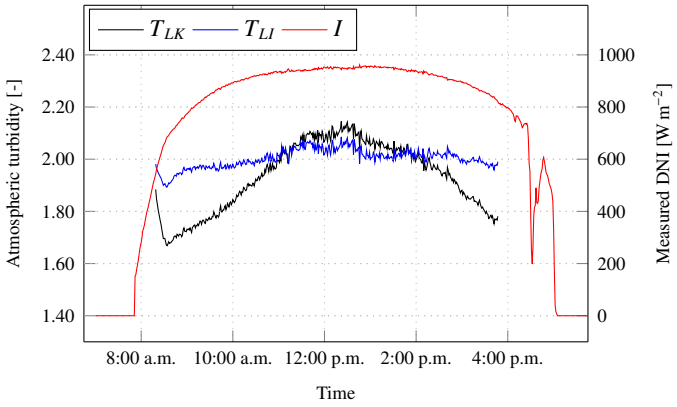

Figure 4: Evolution of both the Kasten-reviewed Linke turbidity coefficient (T_{LK}) and Ineichen atmospheric turbidity coefficient (T_{LI}) during a clear-sky day (PROMES-CNRS database).

As illustrated in Figure 4, T_{LI}, which is relatively stable throughout the day, is less dependent on air mass than T_{LK}. As a result, T_{LI} has been chosen as an input of the models in which the state of the atmosphere is taken into consideration (Section 3.2). Because, in the proposed approach, estimation of the clear-sky DNI is based on the persistence of atmospheric turbidity during the day, T_{LI} is also the best candidate (Section 3.3). In case of clear-sky conditions, it can be easily derived from broadband beam irradiance measurements.

3.2. Approaches included in the comparative study

Overall, we considered five approaches with four of them based on the selected clear-sky DNI models (Section 3.1) and different ways of computing T_{LI}. The first one is the polynomial expression described by Eq. (9), with $\hat{I}_{cs}^{poly}$ the corresponding clear-sky DNI (Eq. (19)):

$$\hat{I}_{cs}^{poly} = \sum_{n=0}^{N} a_n \cdot (\cos z)^n \tag{19}$$

The next two approaches are based on the ESRA model (Eq. (15)), with monthly ($\langle T_{LI}\rangle_m$) or daily ($\langle T_{LI}\rangle_d$) mean values of atmospheric turbidity serving as inputs of the model (Eq. (20)):

$$\hat{I}_{cs}^{ESRA} = I_0 \cdot \exp\left(-0.8662 \cdot m_p \cdot \delta_{cda} \cdot \langle T_{LI}\rangle_{m/d}\right) \tag{20}$$

Two other approaches based on the model developed by Ineichen and Perez (Eq. (16)) are considered in the present study. As in the approaches based on the ESRA model, monthly ($\langle T_{LI}\rangle_m$) or daily ($\langle T_{LI}\rangle_d$) mean values of atmospheric turbidity are used as inputs of the model (Eq. (21)):

$$\hat{I}_{cs}^{Ineichen} = b \cdot I_0 \cdot \exp\left(-0.09 \cdot m\left(\langle T_{LI}\rangle_{m/d} - 1\right)\right) \tag{21}$$

3.3. Proposed approach

The approach proposed to the real-time assessment of the clear-sky DNI comes from the combination of the same model, developed by Ineichen and Perez (Eq. (16)), with a new methodology for the computation of atmospheric turbidity at each time step (this methodology is described in Section 6). The corresponding atmospheric turbidity is called $T_{LI}^{\star}$ (Eq. (22)):

$$\hat{I}_{cs}^{Ineichen} = b \cdot I_0 \cdot \exp\left(-0.09 \cdot m\left(T_{LI}^{\star} - 1\right)\right) \tag{22}$$

4. Experimental data

To evaluate the accuracy of the considered approaches, we used one-minute data from two experimental sites, covering twelve-month periods. The first database comes from the Measurement and Instrumentation Data Center (MIDC). The MIDC makes available irradiance and meteorological data from more than thirty stations in the United States. In the present study, we focused on data from the BMS (Baseline Measurement System) station which is located near Golden (Colorado), at the NREL (National Renewable Energy Laboratory) (Andreas and Stoffel, 1981). This station is situated on a high plain (elevation is about 1800 m), near mountains reaching about 3000 m high.

Table 2: Characteristics of the two experimental sites.

Characteristics	Golden, USA	Perpignan, France
Laboratory	NREL	PROMES-CNRS
Time zone	GMT-7	GMT+1
GPS	39.74 N, 105.18 W	42.66 N, 2.91 E
Altitude	1829 m	50 m
Period of acquisition	01/01/13–31/12/13	01/11/13–31/10/14
Time step	60 s	60 s
Device used for DNI measurement	Pyrheliometer	Rotating shadowband irradiometer
Typical uncertainty	±2%	±5%
Yearly turbidity	2.37	2.61

(a) Pyrheliometer (Golden, USA)

(b) RSI (Perpignan, France)

Figure 5: The pyrheliometer and rotating shadowband irradiometer (RSI) used to measure direct normal irradiance in Golden and Perpignan, respectively.

The second database is derived from measurements realized in Perpignan, at the PROMES-CNRS laboratory. This station is located in Southern France, approximately 20 km west of the Mediterranean sea. Winter is mild and summer is hot and dry. In addition, there is a lot of wind, resulting in a clean atmosphere and a cloudless sky. The main characteristics of these two sites are presented in Table 2. Note that the DNI measurements have been obtained using different devices from the same company (CSP Services, 2015): the NREL uses a pyrheliometer, whereas the PROMES-CNRS laboratory uses a rotating shadowband irradiometer (Figure 5). The typical uncertainties are about ±2% for the pyrheliometer and ±5% for the RSI. However, they are clearly higher at both sunrise and sunset, i.e. when DNI is relatively low. Other data like the air mass or solar angles have been directly extracted from the database (NREL) or computed (PROMES-CNRS).

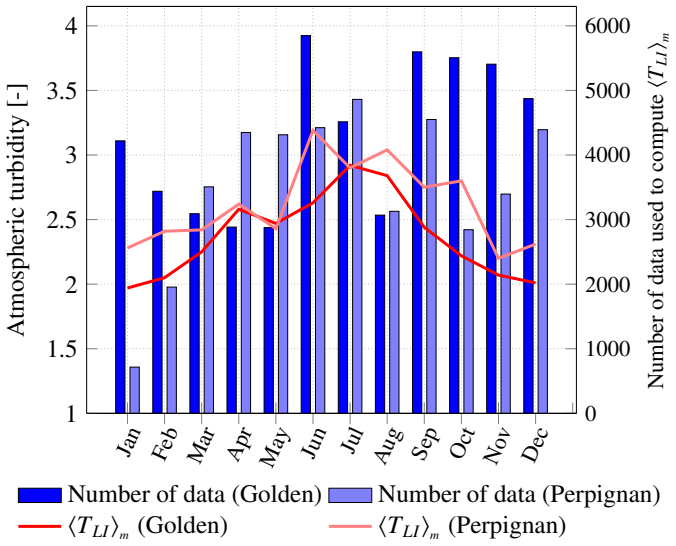

Figure 6: Monthly mean values of atmospheric turbidity ($\langle T_{LI} \rangle_m$) and number of clear-sky DNI data involved in the computation.

Depending on the location, the dynamics of direct normal irradiance as well as the fluctuations one can observe in atmospheric turbidity are rather different. During the twelve-month periods we considered (see Table 2), about 850 h and 700 h of clear-sky DNI data have been detected in Golden and Perpignan, respectively. Note that, with the exception of both January and February months in Perpignan, the number of clear-sky DNI data involved in the computation of T_{LI} is higher than 2000, which is enough to obtain representative monthly mean values of atmospheric turbidity (Figure 6). One can also observe that this quantity is higher in summer than in winter, wathever the site. Overall, atmospheric turbidity is higher in Perpignan, probably because of a higher concentration in particles than in Golden (remember that the BMS station elevation is about 1800 m whereas Perpignan is more or less at sea level).

5. Detection of clear-sky DNI data

To develop and validate the proposed approach, performing an effective detection of clear-sky DNI data in each database is necessary. In a previous work (Nou et al., 2014), a multi-resolution analysis has been used to perform the data detection. This analysis is based on the discrete wavelet transform and allows a signal to be decomposed into approximations (i.e. low-frequency coefficients) and details (i.e. high-frequency coefficients) using a bank of filters composed of low-pass and high-pass filters (Mallat, 2009). Using the discrete wavelet transform, the temporal characteristics of the signal are preserved. This process can be repeated L times, which produces L levels of decomposition, but decomposing the approximations only.

Figure 7 shows the decomposition of level L of a signal x. This signal is first decomposed into an approximation A_1 and a detail D_1 (level 1 of the decomposition). Then A_1 can be

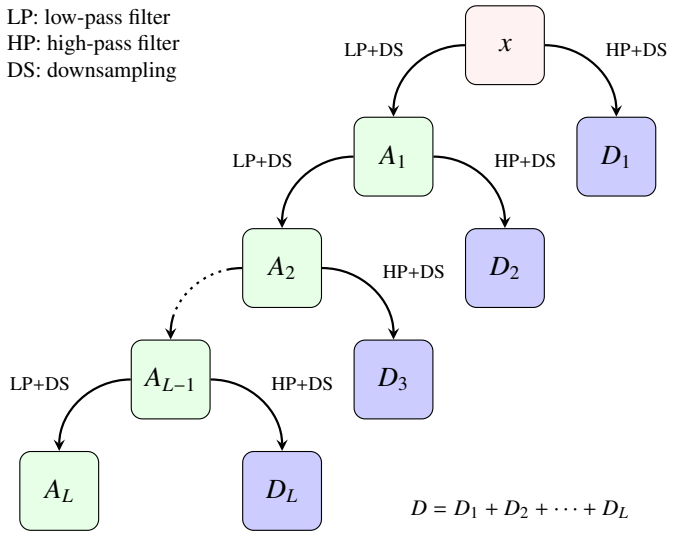

Figure 7: Wavelet-based multi-resolution analysis leading to the decomposition of level L of a signal x.

decomposed into an approximation A_2 and a detail D_2 (level 2 of the decomposition) and so on. As a result, considering L levels of decomposition, the signal x is decomposed into L approximations and L details. The clear-sky data detection process is mainly based on D, defined as the sum of all details (Eq. (23)):

$$D(t) = D_1(t) + D_2(t) + \cdots + D_L(t) \tag{23}$$

Because D reflects the DNI variability, its value is useful to detect small changes in DNI and, as a result, the clear-sky periods. Different families of wavelets may be chosen for analyzing sequences of data points. The main criteria are: the speed of convergence to 0 when the time or the frequency goes to infinity, which quantifies both time and frequency localizations, the symmetry, the number of vanishing moments of the mother wavelet, and the regularity, which is useful for getting nice features, like smoothness of the reconstructed signal. The most commonly used wavelets are the orthogonal ones: Daubechies, Symlet or Coiflet wavelets. Because the Daubechies wavelets have the highest number of vanishing moments (Daubechies et al., 1992), this family has been chosen for carrying out the wavelet-based multi-resolution analysis of the considered sequences of data points.

Although this algorithm was validated in a previous study (Nou et al., 2014), some improvements have been realized in order to detect clear-sky DNI data with a higher accuracy. Limitations of the algorithm occurred in case of some very cloudy periods. Indeed, when the measured DNI is very low and relatively constant, the sum of all details can be close to zero. As a result, in this unusual case, a cloudy period can be considered as a clear-sky one. To solve this problem, an additional coefficient derived from the computation of atmospheric turbidity is proposed. This coefficient, called *coefficient of turbidity* (C_T), is defined as follows (Eq. (24)):

$$C_T(t) = 1 + \left[\frac{11.1}{m(t)} \cdot \ln\left(\frac{b \cdot I_0}{I(t)}\right)\right] \tag{24}$$

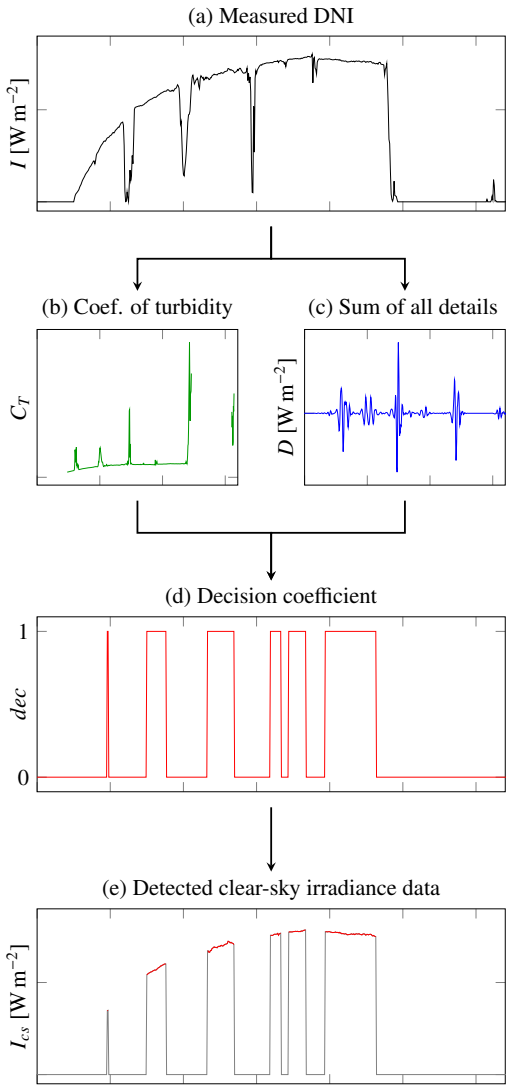

Figure 8: Clear-sky DNI data detection algorithm.

where I is the measured DNI. In fact, once the clear-sky detection using the wavelet-based multi-resolution analysis is performed, the additional coefficient C_T allows some wrong detections to be avoided. Indeed, when C_T is higher than the maximum atmospheric turbidity value measured on-site (T_{max}), the corresponding measured DNI is not considered as a clear-sky DNI. Figure 8 is an example of clear-sky detection performed with the proposed algorithm. First, from the measured DNI I (Figure 8a), the coefficient of turbidity is computed (Figure 8b). Second, I is decomposed into L approximations (not represented) and a detail D, defined as the sum of the L details (Figure 8c). Then, a moving average μ is calculated from D in the following way (Eq. (25)):

$$\mu(t) = \frac{1}{t_w} \sum_{k=t-\frac{1}{2}(t_w-1)}^{t+\frac{1}{2}(t_w-1)} |D(k)| \tag{25}$$

where t_w is the length of the temporal window. Third, a decision coefficient, noted *dec* (Figure 8d), is computed as follows, from

Table 3: Parameters of the clear-sky DNI detection algorithm.

Parameters		Golden	Perpignan
Level of decomposition	L	3	3
Temporal window (min)	t_w	15	15
Threshold (W m^{-2})	μ_{max}	3	5
Maximum turbidity	T_{max}	4.00	4.50

μ and C_T (Eq. (26)):

$$\begin{array}{lll} \text{if} & \mu(t) < \mu_{max} \quad \text{and} \quad C_T(t) < T_{max} & \text{then} \\ & dec(t) = 1 & \\ \text{else} & & \\ & dec(t) = 0 & \\ \text{end} & & \end{array} \tag{26}$$

where T_{max} is the maximum atmospheric turbidity measured on site and μ_{max} (which is defined empirically) is the maximum admissible value for μ. A value of '1' is attributed to dec in case of clear sky conditions whereas '0' is attributed to this parameter in the opposite case. Finally, from this binary sequence, one can obtain the clear-sky DNI (Figure 8e), which is essential in the development and validation of the proposed approach.

A parametric study dealing with the optimal level of decomposition has been performed for the two sites. To this end, we manually selected clear-sky DNI data over a period of 20 days in both databases, according to the shape of the DNI curves. To evaluate the accuracy of the detection algorithm, we defined an index of clear-sky data detection η_{cs}. This index, formulated as a weighted sum, combines the percentage of clear-sky data missed by the detection algorithm (η_{md}) with the percentage of data incorrectly considered as clear-sky data (η_{id}). Note that because avoiding data to be incorrectly detected is more important than missing clear-sky data, η_{id} has been weighted with a coefficient three times higher than the one assigned to η_{md} (Eq. (27)):

$$\eta_{cs}(L) = \frac{1}{4}\eta_{md}(L) + \frac{3}{4}\eta_{id}(L) \tag{27}$$

The aim is to find the level of decomposition that minimizes η_{cs}. For the Golden site, this index is minimized by considering a level of decomposition equal to 3 ($\eta_{cs}(3) = 2.57\%$). Regarding the Perpignan site, the optimal level of decomposition is the same ($\eta_{cs}(3) = 2.69\%$) (Figure 9). Table 3 summarizes all the parameters of the clear-sky DNI detection algorithm, for both sites.

6. Methodology for the computation of $T^{\star}_{LI}$

The clear-sky DNI model considered as part of the proposed approach is mainly based on the behaviour of atmospheric turbidity (Eq. (22)). It takes advantage of the fact that, in case of clear-sky conditions, changes in atmospheric turbidity are relatively small throughout the day in comparison to changes in DNI. Each time DNI is measured, the corresponding coefficient $C_T(t)$ is calculated using Eq. (24). Then, atmospheric turbidity $T^{\star}_{LI}(t)$ is computed by defining Ω as the greyed out area in Figure 10 and using Eq. (28):

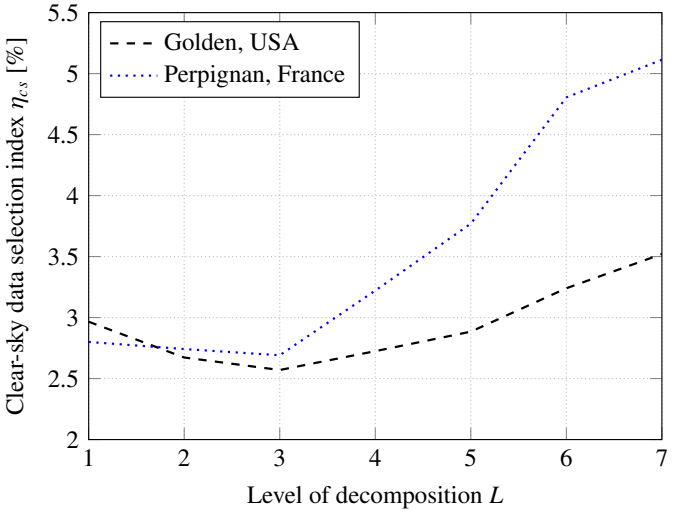

Figure 9: Index of clear-sky data selection η_{cs} as a function of the level of decomposition L.

$$\begin{array}{lll} \text{if} & C_T(t) \in \Omega & \text{then} \\ & T^{\star}_{LI}(t) = C_T(t) & \\ \text{else} & & \\ & T^{\star}_{LI}(t) = T^{\star}_{LI}(t_{past}) & \\ \text{end} & & \end{array} \tag{28}$$

where $T^{\star}_{LI}(t_{past})$ is the last trustable atmospheric turbidity value. Indeed, if the coefficient of turbidity $C_T(t)$ is not inside Ω, it is preferable to keep $T^{\star}_{LI}(t_{past})$ as the new atmospheric turbidity value. At a given time t, the area Ω depends on five parameters (T_{min}, T_{max}, α, β, and ΔT_{max}), defined as follows.

- T_{min} and T_{max} correspond to the minimum and maximum values of atmospheric turbidity $T^{\star}_{LI}$ in the database, respectively. These two parameters are used to make sure that no outlier is computed.
- ΔT_{max} is the largest admissible change in atmospheric turbidity. Because it is a key parameter in the computation of $T^{\star}_{LI}$, it has been set carefully (see Section 8.1.1).
- α represents the maximum growth rate of $T^{\star}_{LI}$ and thus depends on the characteristics of the considered site. It is equal to the slope of the straight line ℓ in Figure 10. As for ΔT_{max}, α is a key parameter in the computation of $T^{\star}_{LI}$. As a result, it has been set carefully (see Section 8.1.1).
- β depends on the accuracy of the DNI measuring device. It can be determined using the absolute difference between two successive estimates of atmospheric turbidity: in the sequel, it is set in a way that 99% of the differences are lower than its value. This threshold is empirically chosen with the aim of limiting the risk of physically impossible changes in atmospheric turbidity.

In Section 8 is explained how to set the values of these five parameters, for both the Golden and Perpignan sites. Finally, at

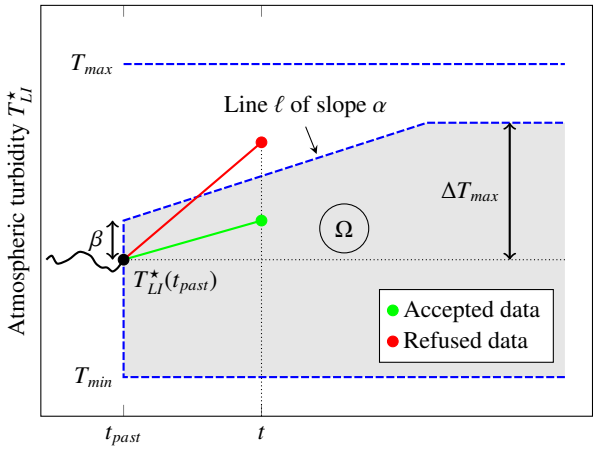

(a) Case where $T^{\star}_{LI}(t_{past}) + \Delta T_{max} < T_{max}$.

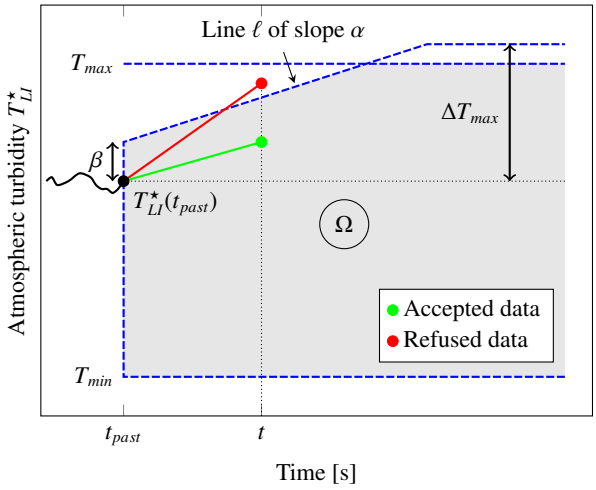

(b) Case where $T^{\star}_{LI}(t_{past}) + \Delta T_{max} > T_{max}$.

Figure 10: Methodology for the computation of atmospheric turbidity ($T^{\star}_{LI}$). Note that case (a) is more probable than case (b) because T_{max} is usually quite high.

a given time t, $T^{\star}_{LI}$ can be expressed through Eqs. (29) and (30):

$$T^{\star}_{LI}(t) \in \left[T_{min},\ \min\left(\ell,\ T^{\star}_{LI}(t_{past}) + \Delta T_{max},\ T_{max}\right)\right] \quad (29)$$

$$\ell = T^{\star}_{LI}(t_{past}) + \alpha(t - t_{past}) + \beta \quad (30)$$

Once $T^{\star}_{LI}$ is known, the clear-sky DNI $\hat{I}_{cs}$ is estimated by using Eq. (22) (Section 3.3).

7. Evaluation procedure and metrics

To estimate the accuracy of the considered approaches, an evaluation procedure has been defined. It is based on the clear-sky DNI data detection presented in Section 5. Starting with a DNI signal of reference, the idea is to simulate changes caused by clouds. The obtained noisy signal I_g can then be used to assess the accuracy of the models: outputs given by the models can be compared with the reference clear-sky DNI values. Figure 11 presents an example of how I_g can be obtained in five steps:

(a) The DNI I is measured.
(b) Using the clear-sky data detection methodology presented in Section 5, the decision coefficient *dec* is determined.
(c) A pseudo-random binary sequence (PRBS) v is generated. The mean value of this PRBS can be adjusted according to the ratio $R_{0/1}$ (e.g. $R_{0/1} = 0.7$ means 70% of '1' (clear-sky data)).
(d) The binary sequence w is obtained by multiplying term by term *dec* and v. Then, w contains only a part of the detected clear-sky periods. The amount of clear-sky periods that are kept can be modulated using $R_{0/1}$.
(e) Finally, the irradiance I_g is computed in the following way (Eq. (31)):

$$\begin{array}{lll} \text{if} & w(t) = 0 & \text{then} \\ & I_g(t) = I(t) & \\ \text{else} & & \\ & I_g(t) = I(t) \cdot k_{rand}(t) & \\ \text{end} & & \end{array} \quad (31)$$

where $k_{rand}(t)$ is a random value between 0 (the Sun is occulted by a thick cloud) and 1 (there is no cloud occulting the Sun). To evaluate the accuracy of the approaches, the Normalized Root Mean Square Error (NRMSE), defined as follows, is used (Eq. (32)):

$$\text{NRMSE} = \frac{\sqrt{\frac{1}{p}\sum\left(I_{cs} - \hat{I}_{cs}\right)^2}}{I_{csmax} - I_{csmin}} \quad (32)$$

where p is the number of data, I_{csmin} and I_{csmax} are the minimum and maximum values of the clear-sky DNI in the database, respectively, and I_{cs} and $\hat{I}_{cs}$ are the detected (from measurements) and estimated values of the clear-sky DNI, respectively. Performance is also evaluated by means of the Mean Absolute Error (MAE), defined by Eq. (33):

$$\text{MAE} = \frac{1}{p}\sum\left|I_{cs} - \hat{I}_{cs}\right| \quad (33)$$

Given that the approach proposed in this paper to the real-time assessment of the clear-sky DNI is mainly based on the behaviour of atmospheric turbidity (see Section 3.3), performance is very dependent on both the considered site (climate, dynamics of atmospheric turbidity...) and accuracy of the measuring device. That is why this approach has been compared with several combinations of existing models and methodologies for the computation of atmospheric turbidity (see Section 3.2).

8. Analysis of the results

This section focuses on tuning the models and evaluating the approaches included in the comparative study thanks to the proposed procedure. Results are discussed in details.

8.1. Tuning of the models

8.1.1. Ineichen and Perez model, with $T^{\star}_{LI}$ used as input

Figure 12 presents, for both the Golden and Perpignan sites, the cumulative distribution of the absolute difference between

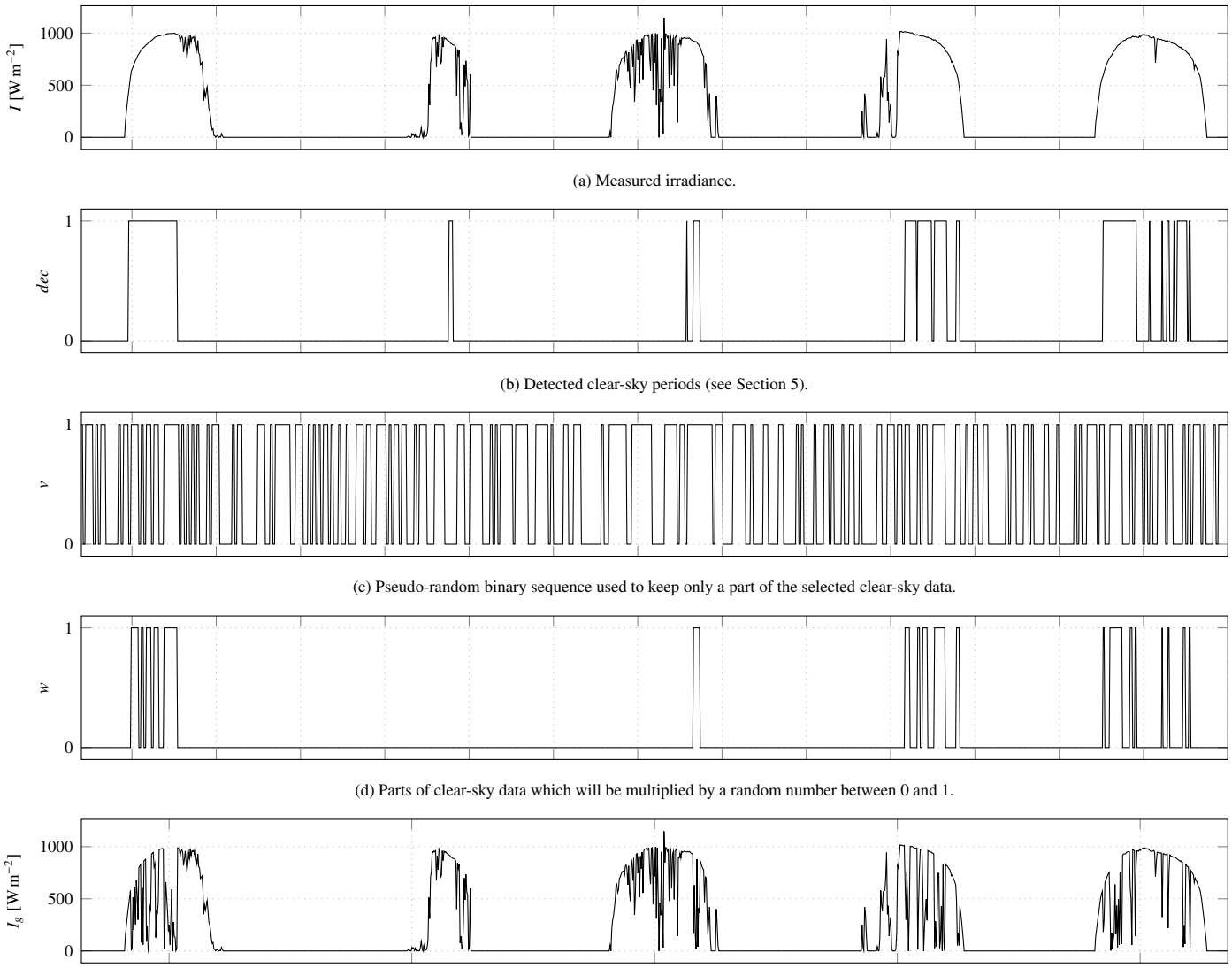

(a) Measured irradiance.

(b) Detected clear-sky periods (see Section 5).

(c) Pseudo-random binary sequence used to keep only a part of the selected clear-sky data.

(d) Parts of clear-sky data which will be multiplied by a random number between 0 and 1.

(e) Noisy irrandiance data used to test the models.

Figure 11: Computation in five steps of I_g (five days from the PROMES-CNRS database).

two successive estimates of atmospheric turbidity. Remember that, according to the methodology proposed for the computation of $T_{LI}^{\star}$ (Section 6), β is set in a way that 99% of the differences are lower than its value. So, we found $\beta = 0.0406$ for Golden and $\beta = 0.0566$ for Perpignan. As one can note, the value we obtained for the Perpignan site is higher than the Golden value. This is probably due to the accuracy of the DNI measuring device, which is affected by the technology: a thermopile is used in Golden whereas the Perpignan site is equipped with a photodiode. Once β is estimated, the couple (α, ΔT_{max}) yielding the lower NRMSE can be determined. Figure 13 presents the NRMSE obtained for different sets of (α, ΔT_{max}). This error is highly dependent on α. In fact, this parameter is mainly affected by the site characteristics, in particular the emissions of gases and particles, and (as for β) the accuracy of the DNI measuring device. For both sites, the parameters allowing $T_{LI}^{\star}$ to be calculated (T_{min}, T_{max}, α, β, and ΔT_{max}) are given in Table 4. As one can note, the accuracy is clearly satisfying: the MAE is less than 10 W m^{-2} whereas the NRMSE does not exceed 1.74%, whatever the site.

Table 4: Parameters for the computation of $T_{LI}^{\star}$ and associated errors.

	Golden, USA	Perpignan, France
T_{min}	1.5	1.5
T_{max}	4.0	4.5
α [s^{-1}]	$1.5 \cdot 10^{-4}$	$0.9 \cdot 10^{-4}$
β	0.0406	0.0566
ΔT_{max}	1.10	1.40
NRMSE	1.74%	1.35%
MAE	9.26 W m^{-2}	8.10 W m^{-2}

8.1.2. Polynomial of the cosine of the solar zenith angle

Regarding the polynomial-based model (Eq. (19)), its coefficients $\{a_n\}_{0 \leqslant n \leqslant N}$ are calculated using the least squares method to fit the clear-sky DNI data we randomly selected in each database (i.e. 5132 data for Golden and 4243 data for Perpignan, which represents one tenth of the available data). Although an order

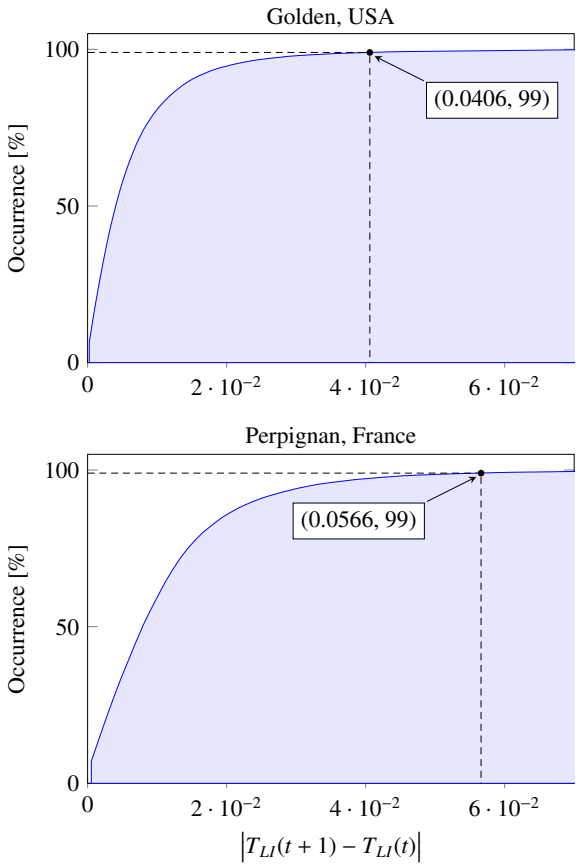

Figure 12: Cumulative distribution of the absolute difference between two successive estimates of atmospheric turbidity, for both the Golden and Perpignan sites. 99% of the differences are lower than the chosen value for β. T_{LI} is estimated from detected clear-sky DNI data (see Section 5), using Eq. (18).

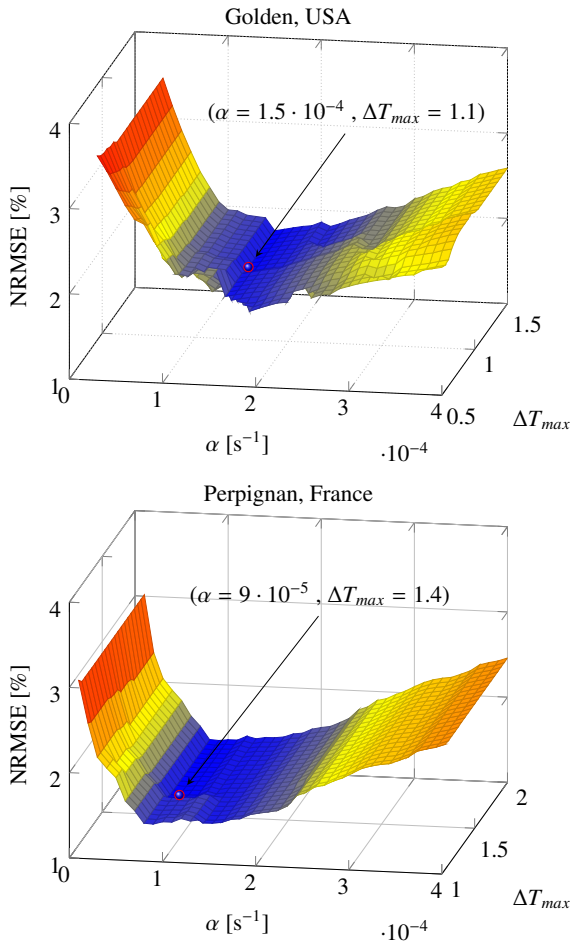

Figure 13: Estimation of the couple (α, ΔT_{max}), for both the Golden and Perpignan sites. The red circles highlight the optimal couples.

$N = 8$ gives the best results (Table 5), a third-order polynomial ($N = 3$) could have been sufficient, as shown by Marquez and Coimbra (Marquez and Coimbra, 2013b). The coefficients we obtained (for $N = 8$) for the Golden (Eq. (34)) and Perpignan (Eq. (35)) sites are, respectively:

$$\{a_n\}_{0\leqslant n\leqslant 8} = 10^3 \cdot \{-0.210, 11.9, -67.5, 216, -336, 124, 307, -392, 138\} \quad (34)$$

$$\{a_n\}_{0\leqslant n\leqslant 8} = 10^3 \cdot \{-1.10, 30.7, -250, 1160, -3160, 5200, -5070, 2700, -606\} \quad (35)$$

8.2. *Evaluation of performance*

The accuracy of all the considered approaches (Eqs. (19) to (22)) has been assessed by means of both the MAE and NRMSE (which are exclusively computed when the binary sequence *dec*, shown in Figure 11, is equal to 1). Table 5 summarizes all the results, for the Golden and Perpignan sites. As expected, both the model developed by Ineichen and Perez and the ESRA model work better than the polynomial-based model (even with $N = 8$), with (either monthly or daily) mean values of atmospheric turbidity (T_{LI}) serving as inputs. Indeed, although all the models take the position of the Sun into account, mean turbidity-based models take advantage of an additional information about the state of the atmosphere. One can note that there is no real benefits in considering daily mean values of atmospheric turbidity, instead of monthly mean values, the errors being very close.

Regarding the proposed approach (Eq. (22)), several values of $R_{0/1}$, ranging from 0.1 to 1, have been tried out. Taking a look at Table 5, one can notice that the more the ratio $R_{0/1}$ increases (i.e. the higher the degradation of the clear-sky DNI signal), the quicker the MAE and NRMSE increase. Indeed, in case of a significant degradation, less data are available to be used in the computation of atmospheric turbidity and, therefore, of the clear-sky DNI. Even with a ratio $R_{0/1}$ set to 1 (which means that all the detected clear-sky DNI data are noisy), the MAE and NRMSE are 25.24 W m^{-2} and 3.45% for the Golden site and 17.61 W m^{-2} and 2.47% for the Perpignan site. Note that in the databases used in the present study, the mean ratio of clear-sky data observed during a day is close to 30%, whatever the site. This corresponds to a ratio $R_{0/1}$ equal to 0.7. So, in that case ($R_{0/1} = 0.7$), the results are satisfying because of a MAE less than 14 W m^{-2} and a maximum NRMSE near to 2.25% in the worst case (i.e. for Golden). Without any doubt, the clear-sky DNI model developed by Ineichen and Perez, combined with the proposed methodology for the computation of atmospheric turbidity (Eq. (22)), offers the lower MAE and NRMSE (even with $R_{0/1} = 1$), in each site.

Table 5: Comparison of the considered approaches, for both the Golden and Perpignan sites. $R_{0/1}$ is the ratio of degradation. N is the polynomial order. Number of clear-sky DNI data considered in the comparative study: 51322 for Golden, USA, and 42432 for Perpignan, France.

Model	Computation of T_{LI}	N or $R_{0/1}$	Golden, USA		Perpignan, France	
			MAE [W m^{-2}]	NRMSE [%]	MAE [W m^{-2}]	NRMSE [%]
$\hat{I}_{cs}^{poly}$	n/a	$N = 2$	88.71	10.51	79.25	10.12
		$N = 3$	63.96	7.42	61.10	7.76
		$N = 4$	63.38	7.14	60.26	7.62
		$N = 5$	63.15	7.09	60.16	7.62
		$N = 6$	62.88	7.06	60.15	7.60
		$N = 7$	62.66	7.03	59.86	7.59
		$N = 8$	62.67	7.03	59.91	7.58
$\hat{I}_{cs}^{ESRA}$	$\langle T_{LI} \rangle_m$	n/a	38.99	4.73	39.83	5.25
	$\langle T_{LI} \rangle_d$	n/a	38.66	4.68	40.86	5.38
$\hat{I}_{cs}^{Ineichen}$	$\langle T_{LI} \rangle_m$	n/a	33.66	4.01	37.61	4.81
	$\langle T_{LI} \rangle_d$	n/a	32.79	3.91	37.86	4.89
	$T_{LI}^{\star}$	$R_{0/1} = 1.0$	25.24	3.45	17.61	2.47
		$R_{0/1} = 0.9$	20.39	2.97	15.20	2.22
		$R_{0/1} = 0.8$	16.22	2.59	12.85	1.96
		$R_{0/1} = 0.7$	13.17	2.25	11.33	1.77
		$R_{0/1} = 0.6$	11.18	2.08	9.59	1.55
		$R_{0/1} = 0.5$	9.26	1.74	8.10	1.35
		$R_{0/1} = 0.4$	7.49	1.47	6.74	1.15
		$R_{0/1} = 0.3$	6.94	1.47	6.49	1.17
		$R_{0/1} = 0.2$	6.30	1.40	5.69	0.97
		$R_{0/1} = 0.1$	5.45	1.13	5.52	0.94

Figure 14 shows an example of results obtained using the considered approaches on three consecutive days in February. Here, no degradation has been applied since real DNI measurements have been used. As a result, Figure 14 highlights from a qualitative point of view how the approaches are able to cope with different DNI behaviours. One can clearly notice, for all days and sites, that the green (i.e. the polynomial-based model), cyan (i.e. the ESRA model with monthly mean values of atmospheric turbidity serving as inputs), and blue (i.e. the Ineichen and Perez model with monthly mean values of atmospheric turbidity serving as inputs) curves are very smooth. However, their profiles are clearly not close to the expected clear-sky DNI profile: they are similar during the three days, since changes in atmospheric turbidity throughout the day are not taken into consideration. Looking at the results we obtained for Golden using the proposed approach (i.e. the Ineichen and Perez model, with atmospheric turbidity being computed as described in Section 6), one can notice, in the first day (February 6), that the red curve follows the measured signal at sunrise, which seems to correspond to a clear-sky period. After the first part of the day (i.e. during the DNI attenuation), the estimated clear-sky DNI has a regular shape, corresponding to an atmospheric turbidity set to the last trustable value ($T_{LI}^{\star}(t) = T_{LI}^{\star}(t_{past})$). This value is kept until the end of the day because no other clear-sky DNI is detected. On the second day (February 7), the model generally follows the measured DNI because it has been detected as a clear-sky DNI. In case of drops in DNI, the model, as expected, does not follow the measurements ($T_{LI}^{\star}(t) = T_{LI}^{\star}(t_{past})$). Finally, on the third day (February 8), because it is totally covered in its first hours (as a result, one can observe very low DNI values), the model starts using as an input the last turbidity of the previous day. Obviously, even if atmospheric turbidity can be quite variable over the days, considering the last turbidity value is statistically better than considering an estimated value given by one of the other approaches. Indeed, these estimated values could not faithfully represent the real state of the atmosphere at a given time. Moreover, using the proposed approach, when the measured DNI is considered as a clear-sky DNI, the atmospheric turbidity value is updated ($T_{LI}^{\star}(t) = C_T(t)$). As a consequence, in that case, the red curve shows a drop in DNI. Although this drop is impossible to observe in case of a clear sky, it corresponds to an accurate update of atmospheric turbidity. Such an adjustment is not available in the other approaches and DNI is provided with a symmetric and smooth shape. Of course, this is incompatible with changes in atmospheric turbidity throughout the day. Note that similar DNI behaviours are observable at Perpignan and Golden, whatever the considered approach. However, the results are not exactly the same, due to local specificities in the dynamics of atmospheric turbidity. Generally, the clear-sky DNI values given by the proposed approach (Eq. (22)) form an upper limit envelope (red curve) and the clear-sky DNI fluctuations, caused by atmospheric turbidity updates, are sometimes not negligible but they are necessary to adapt the model output to an accurate value of the clear-sky DNI. To sum up, the results highlight that the variability of atmospheric turbidity is a key factor to consider in clear-sky DNI estimation.

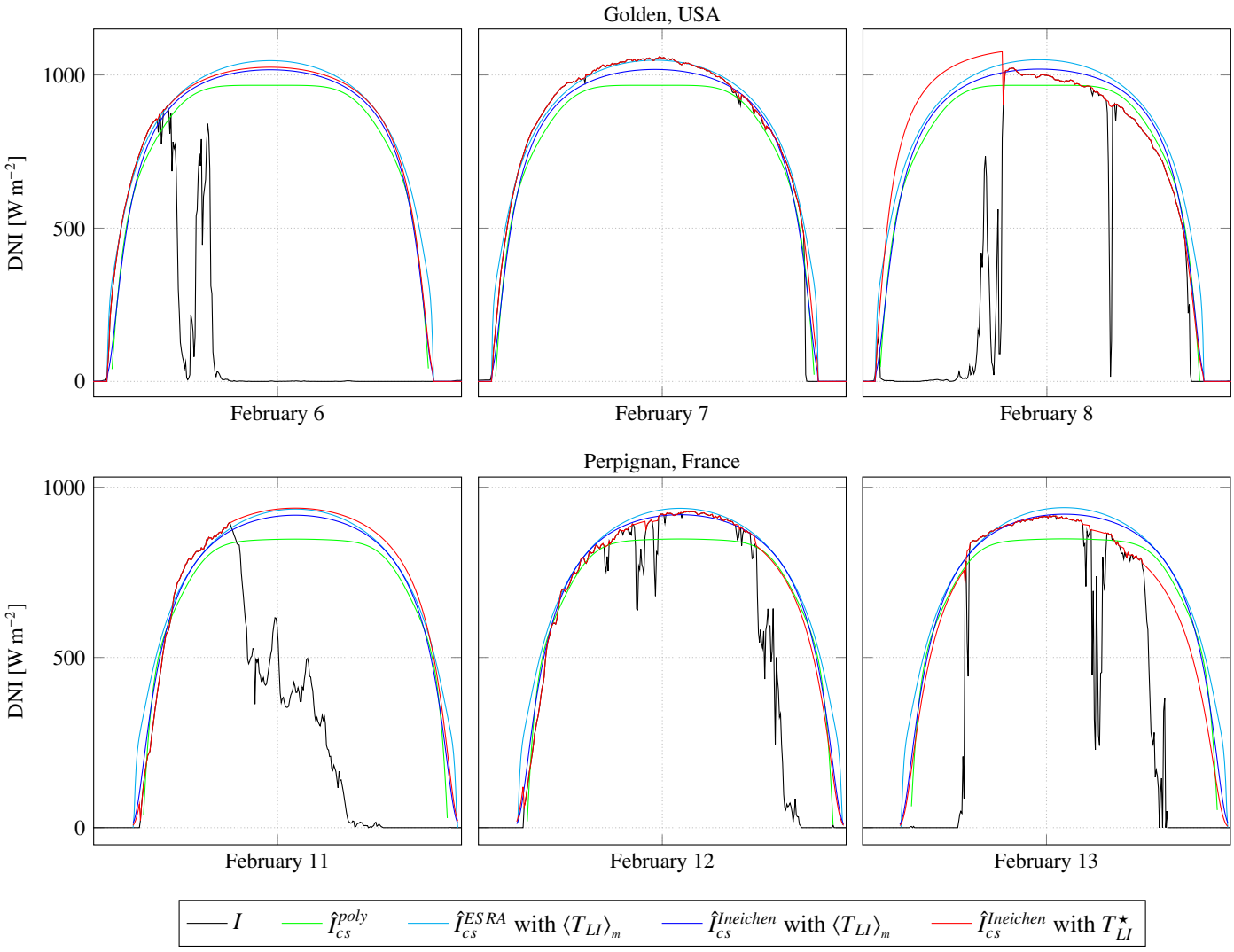

Figure 14: Results obtained using the considered approaches for clear-sky DNI estimation, along with measured DNI in the two experimental sites.

9. Conclusion

In order to achieve a better competitiveness of the concentrating solar power (CSP) technologies and optimize the operation strategies used in the plants, one challenge is to improve solar resource assessment and forecasting. The development of an effective clear-sky DNI model is therefore an essential step in estimating DNI because clear sky defines the nominal operating conditions of the plants. So, the present paper focuses on a new approach to the real-time assessment of the clear-sky DNI. During its development, compromises were made between performance of the algorithms involved and computation time required for their execution. First, for computing the position of the Sun, among the most widely-used algorithms, we opted for SG2 because it is accurate and fast enough. In addition, it allows the Sun-Earth distance to be computed at each time step. As for the computation of the relative optical air mass, among the five functional forms presented, we opted for the widely-used formulation of Kasten and Young. It is very accurate, also at high zenith angles, and its computation time is very low. Regarding the clear-sky DNI model, we decided for the one developed by Ineichen and Perez in 2002. Due to its low dependence on air mass, T_{LI} is relatively stable throughout the day. Note that it is also well adapted to real-time applications. The main contribution of the present work lies in the way atmospheric turbidity is computed and updated in real time. As a key point, we took advantage of the fact that, in case of clear-sky conditions, changes in atmospheric turbidity are relatively small throughout the day in comparison to changes in DNI, even when the sky is free of clouds. So, atmospheric turbidity is computed using the last detected clear-sky DNI measurement.

In the present study, we considered data from two experimental sites (Golden, in the USA, and Perpignan, in France), during one entire year, and used a wavelet-based multi-resolution analysis as a clear-sky DNI detection tool. In addition, we compared the proposed approach with several combinations of empirical models and ways of computing atmospheric turbidity. The first model included in the comparative study is a polynomial of the cosine of the solar zenith angle, whereas the two other models use atmospheric turbidity as an additional input. Regarding its calculation, monthly and daily mean values have been considered. Moreover, we defined a procedure in order to evaluate

the accuracy of all the considered approaches. This procedure allows changes in DNI caused by clouds to be simulated using a noisy signal applied to clear-sky periods. This noisy signal, which is randomly generated, is based on a ratio of degradation $R_{0/1}$. Clear-sky DNI measurements were then used during the validation phase.

It can be noticed that, whatever the approach, the results we obtained using monthly or daily mean values of atmospheric turbidity are always better than those given by the polynomial-based model (even with a relatively high order). Moreover, the proposed approach (i.e. the model developed by Ineichen and Perez, with atmospheric turbidity being computed as described in Section 6) offers unsurpassed accuracy. Indeed, even in the worst case (i.e. $R_{0/1}$ set to 1), the errors one can observe are less than those given by the other approaches. The MAE and NRMSE are 25.24 W m^{-2} and 3.45% for the Golden site and 17.61 W m^{-2} and 2.47% for the Perpignan site, respectively. These highly satisfactory results as well as the compromises we have made between performance and computation time make the proposed approach suitable for real-time applications. As a result, it has just been implemented in a CSP plant (at Palma del Rio, in Spain) and will soon be validated on-site.

Acknowledgements

This work is part of the European project CSPIMP (Concentrated Solar Power efficiency IMProvement), initiated in 2013. This project includes the following partners: General Electric Thermodyn, General Electric Nuovo Pignone, Acciona Energía, ARTS, and PROMES-CNRS.

References

Andreas, A., Stoffel, T., 1981. NREL Solar Radiation Research Laboratory (SRRL): Baseline Measurement System (BMS), Golden, Colorado (Data). URL: http://dx.doi.org/10.5439/1052221.

Arvizu, D., Bruckner, T., Christensen, J., Chum, H., Devernay, J.M., Faaij, A., Fischedick, M., Goldstein, B., Hansen, G., Huckerby, J., Jager-Waldau, A., Kadner, S., Kammen, D., Krey, V., Kumar, A., Lewis, A., Lucon, O., 2011. IPCC Special Report on Renewable Energy Sources and Climate Change Mitigation. Technical Report. IPCC.

Bernecker, D., Riess, C., Angelopoulou, E., Hornegger, J., 2014. Continuous short-term irradiance forecasts using sky images. Solar Energy 110, 303–315.

Blanc, P., Espinar, B., Geuder, N., Gueymard, C., Meyer, R., Pitz-Paal, R., Reinhardt, B., Renné, D., Sengupta, M., Wald, L., Wilbert, S., 2014. Direct normal irradiance related definitions and applications: The circumsolar issue. Solar Energy 110, 561–577.

Blanc, P., Wald, L., 2012. The SG2 algorithm for a fast and accurate computation of the position of the Sun for multi-decadal time period. Solar Energy 86, 3072–3083.

Chauvin, R., Nou, J., Guillot, E., Thil, S., Grieu, S., 2014. Cloud detection methodology based on a sky-imaging system, in: 20th SolarPACES conference, Beijing, China.

Chow, C.W., Urquhart, B., Lave, M., Dominguez, A., Kleissl, J., Shields, J., Washom, B., 2011. Intra-hour forecasting with a total sky imager at the UC San Diego solar energy testbed. Solar Energy 85, 2881–2893.

Chu, Y., Pedro, H.T., Coimbra, C.F., 2013. Hybrid intra-hour DNI forecasts with sky image processing enhanced by stochastic learning. Solar Energy 98, 592–603.

Chu, Y., Pedro, H.T., Li, M., Coimbra, C.F., 2015. Real-time forecasting of solar irradiance ramps with smart image processing. Solar Energy 114, 91–104.

CSP Services, 2015. Solar Resource Assessment MDI, mHP - Plant monitoring MHP Meteorological Measurement Systems for CSP Projects. URL: http://www.cspservices.de/.

Daneshyar, M., 1978. Solar radiation statistics for Iran. Solar Energy 21, 345–349.

Daubechies, I., et al., 1992. Ten lectures on wavelets. volume 61. SIAM.

Davies, J.A., McKay, D.C., 1982. Estimating solar irradiance and components. Solar Energy 29, 55–64.

Duffie, J.A., Beckman, W.A., 1980. Solar engineering of thermal processes. volume 3. Wiley New York etc.

Eltbaakh, Y.A., Ruslan, M.H., Alghoul, M.A., Othman, M.Y., Sopian, K., 2012. Issues concerning atmospheric turbidity indices. Renewable and Sustainable Energy Reviews 16, 6285–6294.

Engerer, N.A., Mills, F.P., 2015. Validating nine clear sky radiation models in Australia. Solar Energy 120, 9–24.

Grena, R., 2008. An algorithm for the computation of the solar position. Solar Energy 82, 462–470.

Grenier, J.C., De La Casinière, A., Cabot, T., 1994. A spectral model of Linke's turbidity factor and its experimental implications. Solar Energy 52, 303–313.

Gueymard, C.A., 1993. Critical analysis and performance assessment of clear sky solar irradiance models using theoretical and measured data. Solar Energy 51, 121–138.

Gueymard, C.A., 2004. The Sun's total and spectral irradiance for solar energy applications and solar radiation models. Solar Energy 76, 423–453.

Gueymard, C.A., 2008. REST2: High-performance solar radiation model for cloudless-sky irradiance, illuminance, and photosynthetically active radiation – validation with a benchmark dataset. Solar Energy 82, 272–285.

Gueymard, C.A., 2012a. Clear-sky irradiance predictions for solar resource mapping and large-scale applications: Improved validation methodology and detailed performance analysis of 18 broadband radiative models. Solar Energy 86, 2145–2169.

Gueymard, C.A., 2012b. Solar radiation, introduction, in: Meyers, R.A. (Ed.), Encyclopedia of Sustainability Science and Technology. Springer New York, pp. 9740–9744.

Gueymard, C.A., 2012c. Temporal variability in direct and global irradiance at various time scales as affected by aerosols. Solar Energy 86, 3544–3553.

Gueymard, C.A., 2013. Aerosol turbidity derivation from broadband irradiance measurements: Methodological advances and uncertainty analysis, in: Solar 2013, American Solar Energy Society, Baltimore, MD.

Gueymard, C.A., Myers, D.R., 2008. Validation and ranking methodologies for solar radiation models, in: Badescu, V. (Ed.), Modeling Solar Radiation at the Earth's Surface. Springer Berlin Heidelberg, pp. 479–510.

Gueymard, C.A., Ruiz-Arias, J.A., 2015. Validation of direct normal irradiance predictions under arid conditions: A review of radiative models and their turbidity-dependent performance. Renewable and Sustainable Energy Reviews 45, 379–396.

Ineichen, P., Perez, R., 2002. A new airmass independent formulation for the Linke turbidity coefficient. Solar Energy 73, 151–157.

Inman, R.H., Edson, J.G., Coimbra, C.F.M., 2015. Impact of local broadband turbidity estimation on forecasting of clear sky direct normal irradiance. Solar Energy 117, 125–138.

Kasten, F., 1980. A simple parameterization of two pyrheliometric formulae for determining the Linke turbidity factor. Meteorologische Rundschau 33, 124–127.

Kasten, F., 1988. Elimination of the virtual diurnal variation of the Linke turbidity factor. Meteorologische Rundschau 41, 93–94.

Kasten, F., 1996. The Linke turbidity factor based on improved values of the integral rayleigh optical thickness. Solar Energy 56, 239–244.

Kasten, F., Young, A.T., 1989. Revised optical air mass tables and approximation formula. Applied Optics 28, 4735–4738.

Laue, E.G., 1970. The measurement of solar spectral irradiance at different terrestrial elevations. Solar Energy 13, 51–57.

Linke, F., 1922. Transmisions-koeffizient und trübungsfaktor. Beiträge zur Physik der Atmosphäre 10, 91–103.

Long, C.N., Ackerman, T.P., 2000. Identification of clear skies from broadband pyranometer measurements and calculation of downwelling shortwave cloud effects. Journal of Geophysical Research - Atmospheres 105, 15609–15626.

Louche, A., Peri, G., Iqbal, M., 1986. An analysis of Linke turbidity factor. Solar Energy 37, 393–396.

Mallat, S., 2009. A wavelet tour of signal processing. 3rd ed., Academic Press.

Marquez, R., Coimbra, C.F.M., 2013a. Intra-hour DNI forecasting based on cloud tracking image analysis. Solar Energy 91, 327–336.

Marquez, R., Coimbra, C.F.M., 2013b. Proposed metric for evaluation of solar forecasting models. Journal of solar energy engineering 135, 011016.

Meinel, A.B., Meinel, M.P., 1976. Applied solar energy: an introduction. Addison-Wesley.

Michalsky, J.J., 1988. The astronomical almanac's algorithm for approximate solar position (1950–2050). Solar Energy 40, 227–235.

Nou, J., Chauvin, R., Traoré, A., Thil, S., Grieu, S., 2014. Atmospheric turbidity forecasting using side-by-side ANFIS. Energy Procedia 49, 2387–2397. Proceedings of the SolarPACES 2013 International Conference.

Paltridge, G.W., Proctor, D., 1976. Monthly mean solar radiation statistics for Australia. Solar Energy 18, 235–243.

Quesada-Ruiz, S., Chu, Y., Tovar-Pescador, J., Pedro, H.T.C., Coimbra, C.F.M., 2014. Cloud-tracking methodology for intra-hour DNI forecasting. Solar Energy 102, 267–275.

Rapp-Arrarás, I., Domingo-Santos, J.M., 2011. Functional forms for approximating the relative optical air mass. Journal of Geophysical Research 116.

Reda, I., Andreas, A., 2003. Solar position algorithm for solar radiation applications. Technical Report. NREL.

Reda, I., Andreas, A., 2004. Solar position algorithm for solar radiation applications. Solar Energy 76, 577–589.

Reno, M., Hansen, C., Stein, J., 2012. Global Horizontal Irradiance Clear Sky Models: Implementation and Analysis. Technical Report. SAND2012-2389, Sandia National Laboratories, Albuquerque, NM and Livermore, CA.

Rigollier, C., Bauer, O., Wald, L., 2000. On the clear sky model of the esra-european solar radiation atlas-with respect to the heliosat method. Solar energy 68, 33–48.

SoDa, 2015. Solar radiation data, solar energy services for professionals. URL: `http://www.soda-is.com/eng/index.html`.

Wald, L., 2007. Solar radiation energy (fundamentals), in: Blanco, J., Malato, S. (Eds.), Solar Energy Conversion and Photoenergy Systems. Encyclopedia of Life Support Systems (EOLSS).

Yang, H., Kurtz, B., Nguyen, D., Urquhart, B., Chow, C.W., Ghonima, M., Kleissl, J., 2014. Solar irradiance forecasting using a ground-based sky imager developed at UC San Diego. Solar Energy 103, 502–524.

Young, A.T., 1994. Air mass and refraction. Applied Optics 33, 1108–1110.

Young, A.T., Irvine, W.M., 1967. Multicolor photoelectric photometry of the brighter planets. I. Program and Procedure. The Astronomical Journal 72, 945.